



## Manganese- and copper-doped titania nanocomposites for the photocatalytic reduction of carbon dioxide into methanol

P.L. Richardson<sup>a</sup>, Marisa L.N. Perdigoto<sup>b</sup>, W. Wang<sup>a</sup>, Rodrigo J.G. Lopes<sup>b,\*</sup>

<sup>a</sup> MSC Catalysis Research Laboratories, California Institute of Technology, Pasadena, CA 91135, USA

<sup>b</sup> CIEPOPF – Centro de Investigação em Engenharia dos Processos Químicos e Produtos da Floresta, GERSE – Group on Environmental, Reaction and Separation Engineering, Department of Chemical Engineering, University of Coimbra, Rua Sílvio Lima, Polo II – Pinhal de Marrocos, 3030-790 Coimbra, Portugal

### ARTICLE INFO

#### Article history:

Received 22 May 2012

Received in revised form 27 June 2012

Accepted 16 July 2012

Available online 22 July 2012

#### Keywords:

Photoreduction

Carbon dioxide

Methanol

XRD

TEM

XPS

### ABSTRACT

In this work, the photocatalytic reduction of CO<sub>2</sub> is comprehensively investigated with commercial and laboratory-made catalysts by doping their surface with an electron acceptor based on Mn and Cu metals. Manganese- and copper-doped titania has been prepared via the sol-gel route as to obtain different nanocomposites for the CO<sub>2</sub> conversion to methanol. First, the XRD characterization demonstrated that both Mn and Cu were finely dispersed on the surface of the titanium oxide support preserving the crystalline structure. Second, the TEM morphological characterization pointed out representative titania grain sizes 15–25 nm as to avoid the surface recombination of electron–hole pairs and concomitantly enhancing the photoactivity. The structural analyses provided by BET and BJH techniques revealed a considerable shrinkage of the volume absorbed for both fresh and used titania specimens when increasing the Mn loading on the TiO<sub>2</sub> substrate, and all the sol-gel derived titania photocatalysts exhibited a mesoporous structure for Mn- and Cu-doped formulations. Afterwards, XPS spectra presented equivalent binding energies characteristic of pure Mn, Cu and Ti (2p<sub>3/2</sub>, 2p<sub>1/2</sub>) by underlining the chemical composition and crystallographic structure of laboratory-made photocatalysts. Finally, several photocatalytic reductions of CO<sub>2</sub> were performed with Mn- and Cu-doped titania catalysts by evaluating the methanol production. The Mn<sub>0.22</sub>–Cu<sub>0.78</sub>/TiO<sub>2</sub> specimen was found to yield a maximum of 238.6 μmol-MeOH/g<sub>cat</sub> with the highest energy (18.4%) and quantum (26.5%) efficiencies thereby acting as a potential candidate catalyst for the photocatalytic conversion of carbon dioxide.

© 2012 Elsevier B.V. All rights reserved.

### 1. Introduction

Carbon dioxide is widely recognized as the main greenhouse gas. The mitigation of global-warming-driven adverse atmospheric phenomena arising from CO<sub>2</sub> generation enjoins actual R&D organizations to properly capture and sequestrate carbon dioxide. As long as CO<sub>2</sub> capture is energy demanding and encompasses an additional cost to be coerced by carbon tax incentives, numerous technologies have been investigated on laboratory and pilot scales. These processes include physisorption/chemisorption [1,2], carbamation [3], amine physical absorption [4], amine dry scrubbing [5], mineral carbonation [6,7], membrane separation [8] and molecular sieves [9]. However, both technologies have insufficient CO<sub>2</sub> capture capacities which need to be overcome on a wider scale for more efficiency but less expensive processes.

Having inherent drawbacks associated with them, alternative, novel and state-of-the-art environmental methodologies

have been receiving emergent interest to efficiently capture and concentrate high-throughputs of carbon dioxide for subsequent conversion into fuels. Provided that CO<sub>2</sub> is rather a stable and an inert compound, the reduction of CO<sub>2</sub> is difficult using conventional ceramic catalysts. The reduction of CO<sub>2</sub> using photocatalysts is regarded as the most prominent methods since CO<sub>2</sub> can be reduced by the UV radiation at room temperatures and atmospheric pressure. In order to respond to the main environmental issues related with global warming and the shortage of sustainable energy sources [10], photoreduction of CO<sub>2</sub> with water has been reported in the literature by dealing with the thermodynamic constraints in the conversion of CO<sub>2</sub> to synthetic fuels such as methane, methanol, formic acid, and formaldehyde [11,12]. This process consists in the catalytic elimination/conversion of this major atmospheric pollutant by providing new insights of heterogeneous catalysis in the realm of environmental pollution abatement.

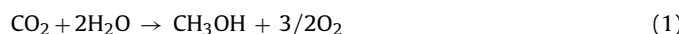
Several semiconductor photocatalysts such as TiO<sub>2</sub>, CdS, WO<sub>3</sub>, ZnO, SiC, and GaP have been used to investigate the photoirradiation of aqueous suspensions when bubbling CO<sub>2</sub>. In the photocatalytic reduction of carbon dioxide, the metal oxides with larger band gaps were identified to be considerably resistant to

\* Corresponding author. Tel.: +351 239798723; fax: +351 239798703.

E-mail address: rodrigo@eq.uc.pt (R.J.G. Lopes).

photocorrosion. In fact,  $\text{TiO}_2$  has been commonly used in heterogeneous photocatalysis for gas- and liquid-phase reactions mainly due to the remarkable physicochemical properties. Various studies on how to increase the photocatalytic activity of  $\text{TiO}_2$  under UV irradiation have been reported with the  $\text{CO}_2$  photoreduction using transition metal doped and/or modified  $\text{TiO}_2$  [11,13–18]. In this regard, copper and iron metals were combined and supported on titanium oxide to evaluate the performance of  $\text{CO}_2$  photoreduction under UVA and UVC irradiation. Multi-walled carbon nanotube-supported  $\text{TiO}_2$  composite catalysts prepared by sol-gel and hydrothermal methods have been investigated for photoreduction of carbon dioxide [19]. Additionally, modified  $\text{TiO}_2$  supported on molecular sieves was evaluated in gas-solid and liquid-solid systems including Ti-MCM-41 [20], Ti-MCM-48 [21], Ti-SBA-15 [22], Ti-HMS [23], Ti-PS [24], Ti-oxide/Y-zeolite catalysts [25].

Typically,  $\text{CO}_2$  is photo-reduced in water vapor or solvent to methanol by photocatalysts as described in Eq. (1):



To the best of our knowledge, the majority of these studies focused on the  $\text{CO}_2$  photoreduction under UV light since the above-mentioned photocatalysts are weakly active under visible light irradiation. Since Mn and Cu metals supported on titanium oxides are scarcely reported for the photocatalytic reduction of  $\text{CO}_2$ , and considering the specific band gap of copper and manganese metals, the respective photocatalyst is envisaged to serve as a benchmark for the photoreduction of carbon dioxide with water. As to obtain high photocatalytic activity, doping the photocatalyst surface with an electron acceptor, Mn–Cu/ $\text{TiO}_2$  nanocomposites are evaluated here for the  $\text{CO}_2$  conversion to methanol. The purpose of this work is twofold: to characterize thoroughly manganese and copper catalysts supported on titanium oxides by transmission electron microscopy (TEM), X-ray diffraction (XRD), X-ray photoelectron spectroscopy (XPS), UV-vis diffused reflectance spectroscopy, and BET/BJH techniques, as well as to evaluate systematically the photocatalytic reduction of  $\text{CO}_2$  querying the effect of nanoparticles load and caustic reaction media conditions.

## 2. Experimental

### 2.1. Materials and preparation of photocatalysts

The titanium oxide powder (P25) was obtained from Degussa.  $\text{TiO}_2$  (P-25) is a nonporous powder formed by a mixture of anatase and rutile (80:20) with a BET surface area of about  $50\text{ m}^2\text{ g}^{-1}$  and average primary particle size of about 30 nm. The precursor was titanium (IV) butoxide ( $\text{Ti}(\text{OC}_4\text{H}_9)_4$ , 98% in *n*-butanol) as supplied from Sigma-Aldrich. Nitrogen was purged in an atmosphere characterized by 20% relative humidity to perform the hydrolysis step. The hydrolyzing water was consistently released by the esterification of butanol and acetic acid in order to circumvent precipitation at the polycondensation stage and also the generation of unstable colloidal sols. This methodology allows one to control the stoichiometric ratio as to carry out the hydrolysis of titanium butoxide with water. 0.01 mol titanium butoxide was then mixed with 0.04 mol anhydrous butanol (>99.7%) and 0.04 mol glacial acetic acid (>99.7%) for a representative batch step and the resulting solution was kept under constant agitation until the pH became constant ( $\approx 3.64$ ). Subsequently, the sol has been dried at  $135^\circ\text{C}$  and further calcinated at  $520^\circ\text{C}$  to remove completely the presence of organic compounds.

The following laboratory-made photocatalysts were prepared via the sol-gel route:  $\text{Mn}/\text{TiO}_2$ ,  $\text{Cu}/\text{TiO}_2$ ,  $\text{Mn}_{0.22}\text{-Cu}_{0.78}/\text{TiO}_2$ ,  $\text{Mn}_{0.51}\text{-Cu}_{0.49}/\text{TiO}_2$ ,  $\text{Mn}_{0.76}\text{-Cu}_{0.24}/\text{TiO}_2$ .  $\text{Mn}(\text{NO}_3)_2\cdot 4\text{H}_2\text{O}$  and

$\text{Cu}(\text{NO}_3)_2\cdot 3\text{H}_2\text{O}$  (Aldrich) have been used as precursors of metal dopants on  $\text{TiO}_2$  support. Manganese- and copper-doped titania ( $\text{Mn}/\text{TiO}_2$ ,  $\text{Cu}/\text{TiO}_2$ ) and  $\text{TiO}_2$  (P25) were impregnated during the sol-gel process. After the calcination stage ( $520^\circ\text{C}$ ), Mn- and Cu-doped titania has been reduced with continuous 6%  $\text{H}_2/\text{Ar}$  stream mixture at  $330^\circ\text{C}$  for 5 h.

### 2.2. Photoreactor and experimental procedure

The catalytic reductions of carbon dioxide were performed in batch operating mode. The photocatalyst powder (0.5 g) was dispersed in a  $\text{CO}_2$  solution (100 ml) in a down-window type irradiation cell made of Pyrex glass. Carbon dioxide was preliminary adsorbed with different aqueous solutions of sodium hydroxide and potassium bicarbonate to enhance  $\text{CO}_2$  solubility. The reactor was fed with pure carbon dioxide (>99.99%) to eliminate the solubilized oxygen from the bulk medium and further saturated with 0.1 M NaOH and 0.25 M  $\text{KHCO}_3$ .

Three different UV lamps were used with the following spectral ranges. Two Hg lamps for near UV (350–450 nm) with 200 W and mid UV (280–350 nm) with 350 W, and a halogen-based lamp for deep UV (240–260 nm) with 500 W HgXe have been evaluated for the photocatalytic conversion of carbon dioxide. Given the wavelength range of the exposure lamps, a cooling system was coupled with a water pump as to keep the reaction system at room temperature. Unless stated otherwise, the photoreduction experiments have been carried out by using the halogen-based lamp for deep UV (240–260 nm) with 500 W HgXe. The wavelength-current spectra of both lamps with an incident light power evaluated at the reactor were: 200 W – 45 mW/cm<sup>2</sup> (410 nm) and 30 mW/cm<sup>2</sup> (370 nm); 350 W – 90 mW/cm<sup>2</sup> (410 nm) and 45 mW/cm<sup>2</sup> (370 nm); 500 W – 20 mW/cm<sup>2</sup> (260 nm). The halogen-based lamp for deep UV (240–260 nm) with 500 W HgXe was typically used for 24 h reaction time and after that, the final reaction products was centrifuged for analyzing them as well as the photocatalysts.

Gas chromatography (TCD/FID) indicated that methanol was the predominant formed hydrocarbon for all the photocatalytic reductions of carbon dioxide so blank experiments were performed to verify the hydrocarbon formation from the  $\text{CO}_2$  conversion. At identical experimental conditions, a blank experiment was carried out under UV irradiation in the absence of catalyst and an additional set was performed with the photocatalyst and carbon dioxide in the dark as to ensure that hydrocarbons were not produced under the above-mentioned trials.

### 2.3. Analytical techniques

Products and reaction intermediates were analytically quantified through gas chromatography (Shimadzu) equipped with a thermal conductivity detector (GC-8A) by using packed columns of molecular sieve 13X-S and polyethylene glycol (PEG-6000) supported on Flusin P 60/80 100 mL (GL Sciences Inc.). The reaction products were also analyzed by gas chromatography (GC-2010 Plus) equipped with a flame ionization detector (ZB-1 column  $T = 170^\circ\text{C}$ , injection  $T = 250^\circ\text{C}$ , determination  $T = 280^\circ\text{C}$ , split ratio 1:300, 0.2  $\mu\text{L}$ ). GC-FID detector is semi-cylindrical electrode type, quartz jet, DL  $3 \times 10^{-12} \text{ g/s}$  for diphenyl,  $T = 450^\circ\text{C}$  in  $1^\circ\text{C}$  increments.

The microstructure and composition of the photocatalysts were analyzed by recording TEM measurements on a JEM 2010 (Jeol) transmission electron microscopy at 200 kV of the acceleration voltage and LaB<sub>6</sub> filament, characterized by 0.23 nm point resolution, convergent-beam and nanobeam diffraction, equipped with Oxford Instruments ATW type EDS detector with INCA Energy TEM platform and elemental mapping using the INCA Semi-STEM mode. Regular single-tilt and double-tilt holders (heating stage <  $1200^\circ\text{C}$

degree) are serviced with a Be double-tilt holder and the tilting limit is  $\pm 30^\circ$ . In all TEM analyzes, the specimens were prepared by suspending solid samples and further ultrasonicated for 20 min.

The textural properties and nitrogen sorption isotherms were determined by the volumetric technique at 77 K using nitrogen by a Micrometrics ASAP 2010 sorptometer. The samples were preliminary submitted to over-drying at 80 °C and evacuated overnight under vacuum condition. The surface area was quantified using Brunauer–Emmett–Teller (BET) surface analysis based on adsorption data in the partial pressure ( $P/P_0$ ) range 0.05–0.95. The amount of nitrogen adsorbed at  $P/P_0 = 0.995$  was used to calculate the total pore volume and the average pore size was found from the adsorption data by Barrett–Joyner–Halenda (BJH) porosity method.

The catalyst crystallinity was characterized by powder X-ray diffraction in a Philips EXPERT  $\theta$ – $2\theta$  X-ray diffractometer with Cu K $\alpha$  radiation ( $\lambda = 1.53 \text{ \AA}$ ) from 20° to 120°  $2\theta$  at a scanning speed of  $0.03^\circ \text{ s}^{-1}$ . The X-ray tube voltage and current were set at 35 kV and 45 mA, respectively. The line broadening of anatase TiO<sub>2</sub> reflection plane ( $2\theta = 48^\circ$ ) has been used to probe the crystallite size pointing out that there was negligible interference from the photocatalysts.

X-ray photoelectron spectroscopy data were recorded with a Thermo VG Scientific Sigma Probe spectrometer using AlK $\alpha$  radiation at 15 kV, 25 mA, pass energy 22.0 eV. The base pressure in the analyzing chamber was preserved in the range of  $2 \times 10^{-8}$ – $6 \times 10^{-9}$  Torr. The binding energy of XPS spectra was adjusted by carbon: 2p<sub>3/2</sub> = 285.0 eV. Depth-profile measurements was additionally performed using Ar<sup>+</sup> etching for 20 min to investigate the core of the Mn- and Cu-doped titania photocatalysts.

UV-visible spectrophotometer (JASCO V-650) has been used to perform optical spectroscopic measurements using D<sub>2</sub> and halogen lamps for wavelengths below and above 335 nm, respectively. The diffuse reflectance measurements were accomplished by means of an integrating sphere (JASCO ISV-469) and the measurements have been recorded at 280 K for wavelengths in the range 200–800 nm with 0.1 g of fresh and used catalysts. The Kubelka–Munk function has been applied to convert the DRS data to absorption spectra, and the Davis–Mott model was used to estimate the bandgap ( $E_g$ ) of the laboratory-made photocatalysts.

### 3. Results

#### 3.1. XRD characterization

The phase structure of fresh and used Mn- and Cu-doped titania photocatalysts have been characterized by means of X-ray diffraction analyses. Fig. 1a and b shows the powder XRD patterns of the fresh and used (24 h reaction time) Mn<sub>0.22</sub>–Cu<sub>0.78</sub>/TiO<sub>2</sub>, respectively. As can be seen, the XRD diffractograms exhibited peaks at 40.3° and 52.8° which can be assigned to the titanium substrate. Indeed, the XRD peaks at 24.9°, 37.3°, 48.7° and 55.2° are from the (1 1 0), (1 0 3), (2 0 0) and (1 0 5) diffractions, respectively, of anatase-phase titanium oxide. The feature diffraction peaks of MnO<sub>2</sub> are 28.7° (1 1 0), 37.4° (1 0 1), 43.0° (1 1 1), 56.8° (2 1 1) and 64.9° (0 0 2). The diffraction peaks at  $2\theta = 29.5^\circ$ , 36.4°, 42.3°, 61.5°, 74.0° and 77.6° can be assigned to the (1 1 0), (1 1 1), (2 0 0), (2 2 0), (3 1 1) and (2 2 2) planes of crystalline cuprous oxide, respectively. X-ray diffraction patterns of both fresh and used catalyst coated as thin films have demonstrated that there is a slight difference between the X-ray diffraction pattern of bare TiO<sub>2</sub> and that of manganese and copper doped TiO<sub>2</sub>.

The XRD diffractograms depicted in Fig. 1a and b indicated the crystal phase of the TiO<sub>2</sub> so the calcination temperature allows obtaining crystalline nanomaterials that were treated in the range from 300 to 520 °C. In what regards the effect of the calcination temperature, a further increase has revealed that

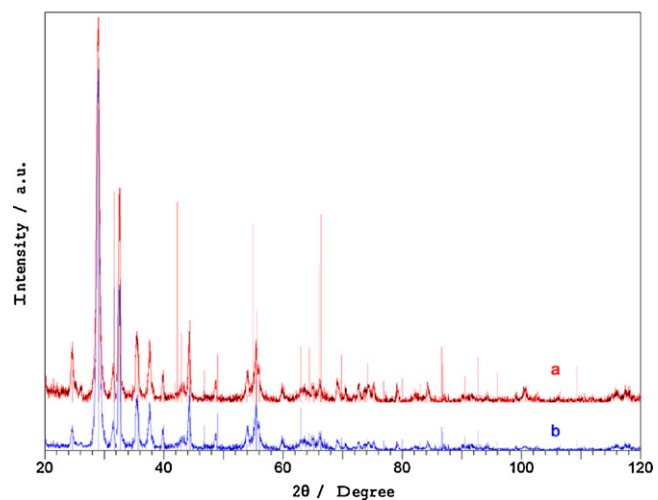


**Fig. 1.** X-ray diffractogram of (a) fresh and (b) used laboratory-made Mn<sub>0.22</sub>–Cu<sub>0.78</sub>/TiO<sub>2</sub> photocatalyst.

it affects negatively the anatase/rutile crystalline phase of the photocatalyst so the laboratory-made become more amorphous. Indeed, a anatase/rutile ratio of 73/27 was obtained for the Mn<sub>0.22</sub>–Cu<sub>0.78</sub>/TiO<sub>2</sub> nanocomposite as can be seen from the diffractograms depicted in Fig. 1. Both fresh and used diffractograms were considerably different for the original titanium oxide calcinated at the same temperature. Accordingly, calcination temperatures higher than 520 °C produced diffraction peaks at 25.1° (1 0 1), 27.3° (1 1 0), 36.5° (1 0 1), 48.4° (2 0 0), 54.1° (2 1 1), and 69.2° (2 2 0). If one increased even further the calcination temperature, the anatase phase (1 0 1) become amorphous and the rutile phase (1 1 0) transformed into dense crystals during severe cure treatments.

#### 3.2. TEM morphological characterization

The TEM patterns of the Mn<sub>0.22</sub>–Cu<sub>0.78</sub>/TiO<sub>2</sub> photocatalyst are shown in Fig. 2 for fresh (a) and used (b) Mn- and Cu-doped titania samples. As can be seen, these images indicated the presence of titania-based catalysts with grain sizes <55 nm. This fact has been confirmed by the Scherrer model so the particle sizes obtained via the sol–gel route were in agreement with the transmission electron microscopy maps depicted in Fig. 2a and b. According to these patterns, the particles of Mn<sub>0.22</sub>–Cu<sub>0.78</sub>/TiO<sub>2</sub> exhibited a quasi-homogeneous size and shape with a diameter between 20 and 35 nm. In addition, the manganese and copper aggregates were homogeneously distributed across the surface of titanium oxide substrate. As expected, Mn and Cu clusters have been deposited on the surface of titania-based framework mainly due to the addition of the precursors of the metal dopants during the photocatalyst preparation once the hydrolysis of titanium butoxide was complete.

As to promote the photocatalytic reduction of carbon dioxide, the typical titania grain size was in the range from 15 to 25 nm. This fact enabled one to avoid the surface recombination of electron–hole pairs which become relevant with particle size diameter in the range 1–15 nm. In fact, the particle size distribution of manganese- and copper-doped titania catalysts has been evaluated and the mean particle sizes were in the range of 55 and 91 nm, while the commercial titanium oxide has revealed a biomodal particle size distribution with the following dominant sizes, 48 and 71 nm.

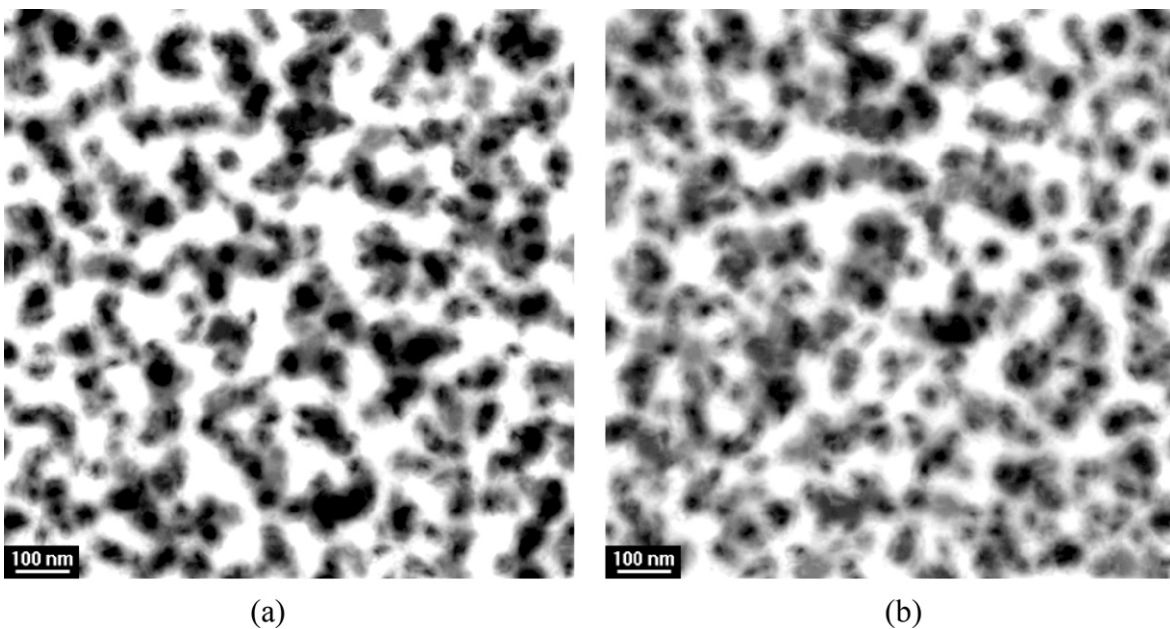


**Fig. 2.** Transmission electron microscopy patterns of (a) fresh and (b) used laboratory-made  $\text{Mn}_{0.22}\text{--Cu}_{0.78}/\text{TiO}_2$  photocatalyst.

### 3.3. BET and BJH analyses

The BET isotherms for the  $\text{Mn}_{0.22}\text{--Cu}_{0.78}/\text{TiO}_2$ ,  $\text{Mn}_{0.51}\text{--Cu}_{0.49}/\text{TiO}_2$ , and  $\text{Mn}_{0.76}\text{--Cu}_{0.24}/\text{TiO}_2$  catalysts before and after 24 h of photocatalytic reductions were determined through the accelerated surface area and porosimetry analyzer. Fig. 3a and c shows the Brunauer–Emmet–Teller isotherms for the manganese- and copper-doped titania catalysts prepared via the sol–gel process with different molar ratios. According to Fig. 3a and c, the shrinkage of the volume absorbed for both fresh and used titania specimens has been ascribed to the increase in manganese loading on the  $\text{TiO}_2$  substrate. The porosity analysis revealed quantitative differences in textural properties amongst the three samples by showing type IV isotherms. From these profiles, all the sol–gel derived titania photocatalysts exhibited a mesoporous structure for Mn- and Cu-doped formulations. Table 1 shows the surface area and pore volume of  $\text{TiO}_2$  (P25),  $\text{Mn}/\text{TiO}_2$ ,  $\text{Cu}/\text{TiO}_2$ ,  $\text{Mn}_{0.22}\text{--Cu}_{0.78}/\text{TiO}_2$ ,  $\text{Mn}_{0.51}\text{--Cu}_{0.49}/\text{TiO}_2$ ,  $\text{Mn}_{0.76}\text{--Cu}_{0.24}/\text{TiO}_2$  prepared with different molar proportions as well as the crystal sizes and bandgap energies of the manganese- and copper-doped photocatalysts. The total pore volume was determined by the adsorption at a relative pressure of 0.995 for  $\text{N}_2$  at 77 K. The highest surface area was for the commercial catalyst ( $\text{TiO}_2$  P25,  $50 \text{ m}^2 \text{ g}^{-1}$ ), while the lower was obtained for the laboratory-made  $\text{Mn}_{0.22}\text{--Cu}_{0.78}/\text{TiO}_2$  with  $22 \text{ m}^2 \text{ g}^{-1}$ .

Fig. 4a and c plots the pore size distribution of the  $\text{Mn}_{0.22}\text{--Cu}_{0.78}/\text{TiO}_2$ ,  $\text{Mn}_{0.51}\text{--Cu}_{0.49}/\text{TiO}_2$ , and  $\text{Mn}_{0.76}\text{--Cu}_{0.24}/\text{TiO}_2$  catalysts before and after 24 h of photocatalytic reductions. Both

fresh and used specimens have somewhat narrow pore size distribution with identical mean pore sizes (29–36 nm) and became slightly wider as the manganese loading increases. In addition, the reduction of surface area when doping the  $\text{TiO}_2$  substrate with more manganese can be attributed to the contraction of the porous coating. From the tabulated data, the Mn- and Cu-doped photocatalysts had analogous BJH properties concerning the pore volume of  $\text{Mn}_{0.22}\text{--Cu}_{0.78}/\text{TiO}_2$ ,  $\text{Mn}_{0.51}\text{--Cu}_{0.49}/\text{TiO}_2$ , and  $\text{Mn}_{0.76}\text{--Cu}_{0.24}/\text{TiO}_2$  compared to commercial  $\text{TiO}_2$  (P25). The higher crystal size is probably due to the more condensed structure of titanium oxide shell so it was further affected by the stoichiometric ratio of Ti/O during the catalyst preparation via the sol–gel route. This fact can be identified from the analysis of the TEM patterns shown in Fig. 2a and b for the  $\text{Mn}_{0.22}\text{--Cu}_{0.78}/\text{TiO}_2$  specimen. Therefore, the  $\text{Mn}/\text{TiO}_2$  had smaller crystal sizes comparatively to the crystals of  $\text{Cu}/\text{TiO}_2$  leading to different BET surface areas mainly due to the spatial arrangement of the metal dopants on the titania substrate.

### 3.4. XPS characterization and chemical composition

The chemical composition of  $\text{Mn}_{0.22}\text{--Cu}_{0.78}/\text{TiO}_2$ ,  $\text{Mn}_{0.51}\text{--Cu}_{0.49}/\text{TiO}_2$ , and  $\text{Mn}_{0.76}\text{--Cu}_{0.24}/\text{TiO}_2$  catalysts has been characterized by means of X-ray photoelectron spectroscopy. Fig. 5a shows the spectra of Mn ( $2p_{3/2}$ ,  $2p_{1/2}$ ) of catalysts, respectively; while Fig. 5b displays the spectra of Ti ( $2p_{3/2}$ ,  $2p_{1/2}$ ) catalysts, and Fig. 5c depicts the XPS spectra of Cu ( $2p_{3/2}$ ,  $2p_{1/2}$ ) specimens. The binding energies of Mn  $2p_{3/2}$  and  $2p_{1/2}$  were 641.6 and 652.9 eV for all manganese- and copper-doped titania catalysts ( $\text{Mn}_{0.22}\text{--Cu}_{0.78}/\text{TiO}_2$ ,  $\text{Mn}_{0.51}\text{--Cu}_{0.49}/\text{TiO}_2$ ,  $\text{Mn}_{0.76}\text{--Cu}_{0.24}/\text{TiO}_2$ ). Correlating the XPS spectra with the crystallographic structure discussed in Fig. 1, these laboratory-made photocatalysts presented roughly the same binding energies characteristic of manganese oxide which indicated that this metal was crystallized predominantly as  $\beta\text{-MnO}_2$  (see Fig. 1 and Fig. 5a). Moreover, the impregnation of Mn as a metal dopant for the titania substrate was found to have no significant influence on the crystalline framework of  $\text{TiO}_2$ , as can be seen from Fig. 5b. The XPS spectra of Ti ( $2p_{3/2}$ ,  $2p_{1/2}$ ) for both fresh and used photocatalysts unveiled identical binding energies that are relative to those of pure titanium oxide at 459.2 and 464.9 eV. This fact underlined the

**Table 1**

Brunauer–Emmet–Teller surface area ( $S_{\text{BET}}$ ), pore volume ( $V_{\text{pore}}$ ), crystal sizes and bandgap energies of  $\text{TiO}_2$  (P25) and manganese- as well as copper-doped titania photocatalysts prepared with different molar proportions.

	$S_{\text{BET}}$ ( $\text{m}^2 \text{ g}^{-1}$ )	$V_{\text{pore}}$ ( $\text{cm}^3 \text{ g}^{-1}$ )	$d_{\text{crystal}}$ (nm)	$E_g$ (eV)
$\text{TiO}_2$ (P25)	50	–	23	3.48
$\text{Mn}/\text{TiO}_2$	42	0.032	17	3.24
$\text{Cu}/\text{TiO}_2$	31	0.028	21	2.88
$\text{Mn}_{0.22}\text{--Cu}_{0.78}/\text{TiO}_2$	22	0.021	14	2.93
$\text{Mn}_{0.51}\text{--Cu}_{0.49}/\text{TiO}_2$	27	0.024	18	2.96
$\text{Mn}_{0.76}\text{--Cu}_{0.24}/\text{TiO}_2$	29	0.026	10	3.07

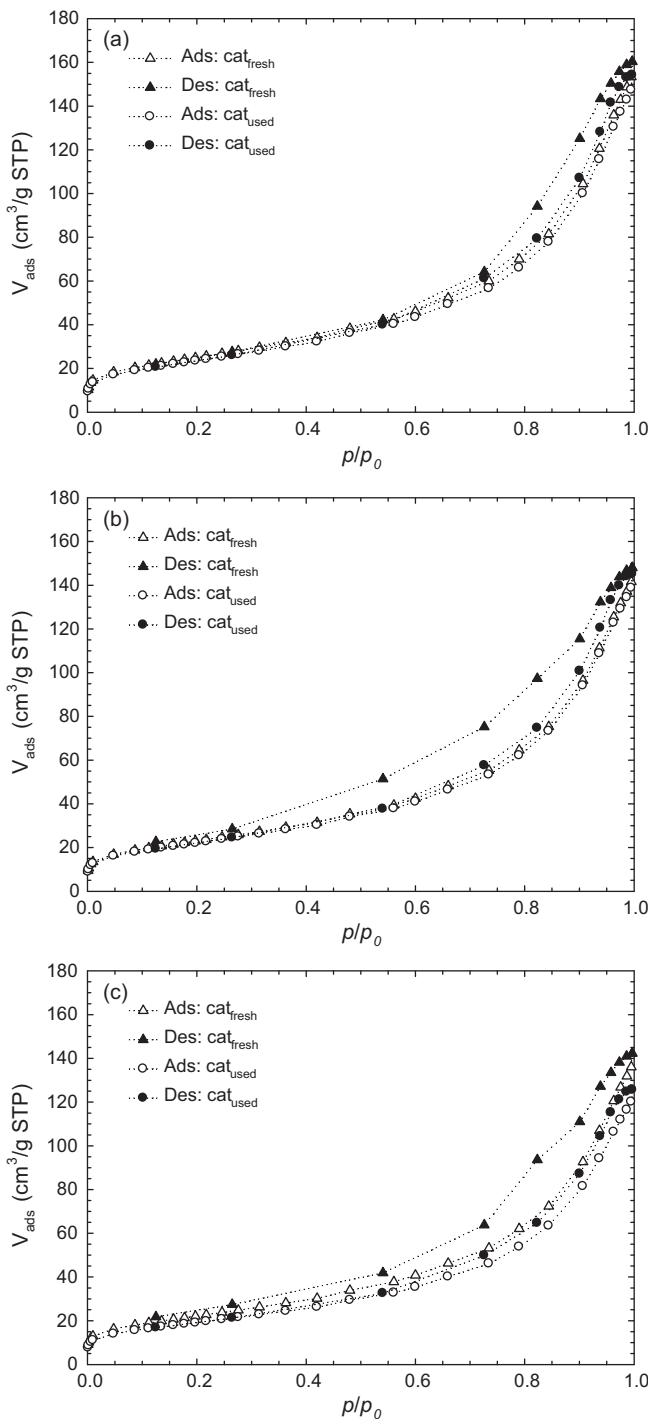


**Fig. 3.** Brunauer–Emmet–Teller isotherm of (a)  $\text{Mn}_{0.22}\text{-Cu}_{0.78}/\text{TiO}_2$ , (b)  $\text{Mn}_{0.51}\text{-Cu}_{0.49}/\text{TiO}_2$ , (c)  $\text{Mn}_{0.76}\text{-Cu}_{0.24}/\text{TiO}_2$  photocatalysts.

crystallographic structure of  $\text{TiO}_2$  that was maintained after the doping process with manganese and copper metals. Indeed, Fig. 5c shows the XPS spectra of Cu ( $2p_{3/2}$ ,  $2p_{1/2}$ ) and the characteristic binding energies at 933.3 and 953.1 eV pointing out the presence of  $\text{Cu}_2\text{O}$  species supported on the surface of titania substrate based catalysts.

The element molar ratios of manganese- and copper-doped photocatalysts calculated from X-ray photoelectron spectroscopy are shown in Table 2, where the bulk information is relative to the photocatalyst preparation via the sol–gel route. While the chemical composition given by XPS spectra corresponds to exterior surface

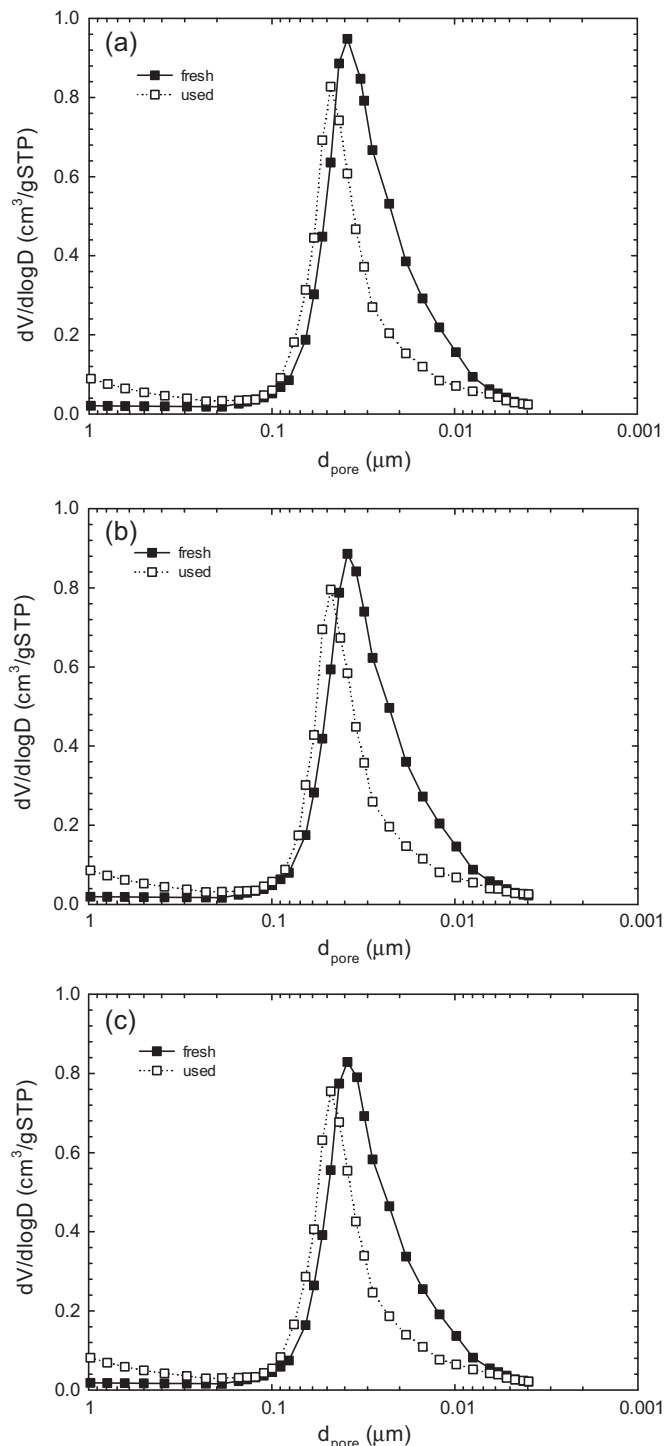


**Fig. 4.** Porosity size distribution of (a)  $\text{Mn}_{0.22}\text{-Cu}_{0.78}/\text{TiO}_2$ , (b)  $\text{Mn}_{0.51}\text{-Cu}_{0.49}/\text{TiO}_2$ , (c)  $\text{Mn}_{0.76}\text{-Cu}_{0.24}/\text{TiO}_2$  photocatalysts.

**Table 2**

Chemical composition and element molar ratio of manganese- and copper-doped photocatalysts calculated from X-ray photoelectron spectroscopy.

	Mn/Ti		Cu/Ti		Mn/Cu	
	XPS	Bulk	XPS	Bulk	XPS	Bulk
Mn/TiO <sub>2</sub>	0.239	0.052	–	–	–	–
Cu/TiO <sub>2</sub>	–	–	0.194	0.044	–	–
Mn <sub>0.22</sub> -Cu <sub>0.78</sub> /TiO <sub>2</sub>	0.047	0.011	0.162	0.041	0.290	0.268
Mn <sub>0.51</sub> -Cu <sub>0.49</sub> /TiO <sub>2</sub>	0.098	0.025	0.104	0.022	0.942	1.136
Mn <sub>0.76</sub> -Cu <sub>0.24</sub> /TiO <sub>2</sub>	0.134	0.046	0.045	0.013	2.978	3.538

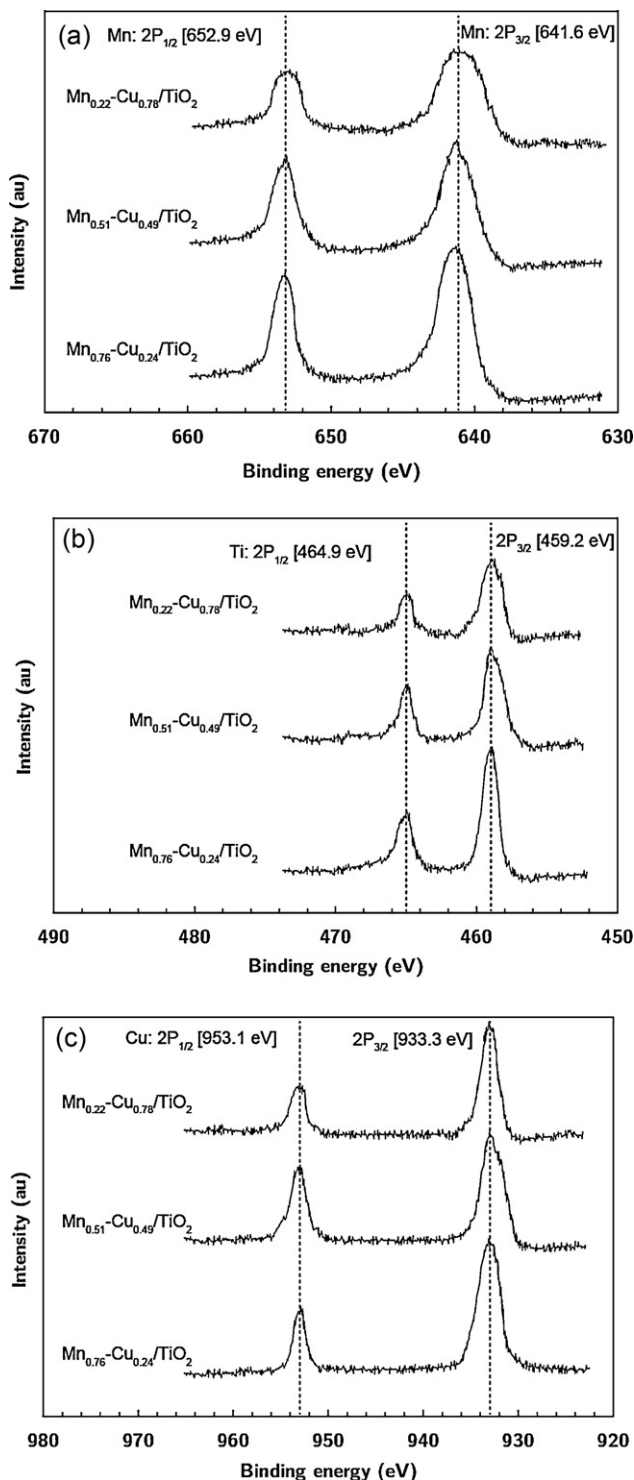


**Fig. 5.** X-ray photoelectron spectra of (a) Mn 2p, (b) Ti 2p, and (c) Cu 2p in Mn<sub>0.22</sub>-Cu<sub>0.78</sub>/TiO<sub>2</sub>, Mn<sub>0.51</sub>-Cu<sub>0.49</sub>/TiO<sub>2</sub>, Mn<sub>0.76</sub>-Cu<sub>0.24</sub>/TiO<sub>2</sub> photocatalysts.

of the specimen being analyzed, the bulk characterization accounts for the deep and whole photocatalyst structure including the titania substrate/backbone. This fact explained how different the chemical composition and element molar ratios of Mn/TiO<sub>2</sub>, Cu/TiO<sub>2</sub>, Mn<sub>0.22</sub>-Cu<sub>0.78</sub>/TiO<sub>2</sub>, Mn<sub>0.51</sub>-Cu<sub>0.49</sub>/TiO<sub>2</sub>, Mn<sub>0.76</sub>-Cu<sub>0.24</sub>/TiO<sub>2</sub> photocatalysts are from the comparison between the bulk data and the XPS spectra.

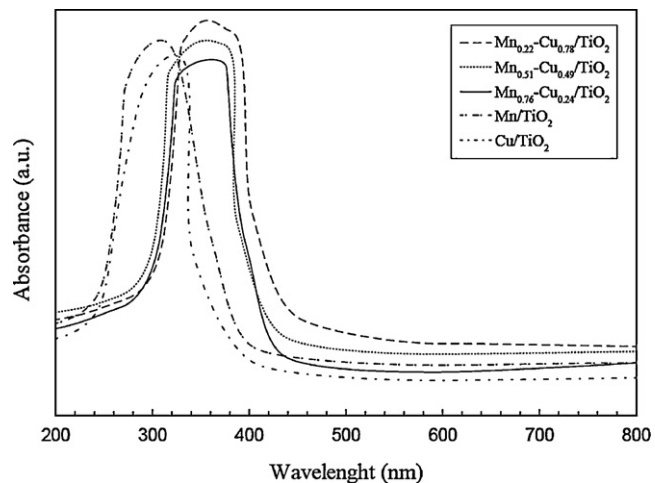


**Fig. 6.** UV-vis spectra of Mn<sub>0.22</sub>-Cu<sub>0.78</sub>/TiO<sub>2</sub>, Mn<sub>0.51</sub>-Cu<sub>0.49</sub>/TiO<sub>2</sub>, Mn<sub>0.76</sub>-Cu<sub>0.24</sub>/TiO<sub>2</sub> photocatalysts.

### 3.5. Diffuse reflectance spectroscopy

The manganese- and copper-doped titania photocatalysts have been analyzed by means of UV-vis diffuse reflectance spectroscopy as to gather further insights into the absorption of UV and visible light by the laboratory-made catalysts. As depicted in Fig. 6, the DRS spectra indicate that both metal dopants allow preserving the light absorption capacity of titanium oxide as shown for both Mn<sub>0.22</sub>-Cu<sub>0.78</sub>/TiO<sub>2</sub>, Mn<sub>0.51</sub>-Cu<sub>0.49</sub>/TiO<sub>2</sub>, and Mn<sub>0.76</sub>-Cu<sub>0.24</sub>/TiO<sub>2</sub> specimens. Both manganese- and copper-doped titania catalyst exhibited a maximum absorption intensity in the range 340–360 nm. According to Table 1, the higher bandgaps were obtained for TiO<sub>2</sub> (P25) and Mn/TiO<sub>2</sub> with 3.48 and 3.24 eV, respectively; whereas the laboratory-made catalysts including Cu/TiO<sub>2</sub>, Mn<sub>0.22</sub>-Cu<sub>0.78</sub>/TiO<sub>2</sub>, Mn<sub>0.51</sub>-Cu<sub>0.49</sub>/TiO<sub>2</sub>, Mn<sub>0.76</sub>-Cu<sub>0.24</sub>/TiO<sub>2</sub> exhibited bandgaps lower than 3 eV, except for the last one. One should bear in mind that the crystalline structure of titanium oxides may be dictated the bandgap, which can be also linked with the heterogeneous structure of titania photocatalysts when synthetized via the sol-gel route.

### 3.6. Photocatalytic reduction of carbon dioxide

The catalytic activity of Mn- and Cu-doped titania catalysts was evaluated in terms of methanol production. Fig. 7 shows the temporal evolution of methanol yield as a function of reaction time for the commercial and laboratory-made photocatalysts (0.5 g/L) prepared via the sol-gel route. As can be seen for 10 h reaction time, the methanol yields were 137.5, 120.3, 105.4, 98.1, 83.7, and 74.4 μmol/g<sub>cat</sub> for Mn<sub>0.22</sub>-Cu<sub>0.78</sub>/TiO<sub>2</sub>, Mn<sub>0.51</sub>-Cu<sub>0.49</sub>/TiO<sub>2</sub>, Mn<sub>0.76</sub>-Cu<sub>0.24</sub>/TiO<sub>2</sub>, Cu/TiO<sub>2</sub>, Mn/TiO<sub>2</sub>, TiO<sub>2</sub> (P25), respectively. From these experimental data, the photocatalytic reduction of carbon dioxide was found to be efficiently promoted when using manganese and copper-doped titania catalysts. In fact, all Mn-Cu/TiO<sub>2</sub> photocatalysts gave the higher CO<sub>2</sub> conversions as compared to the commercial sample. Even the Cu/TiO<sub>2</sub> revealed superior performance in comparison to TiO<sub>2</sub> (P25) catalyst. After 24 of irradiation time, the photocatalytic yields in terms of methanol were significantly higher as follows: 238.6, 203.8, 186.4, 172.0, 159.8, and 151.6 μmol/g<sub>cat</sub>.

The CO<sub>2</sub> conversions attained with the laboratory-made catalysts are directly related with the preparation methodology so the photocatalytic structure of titania substrate and the corresponding metal dopant exhibited different spatial mappings of electric charge. The electronic configuration of copper aggregates is

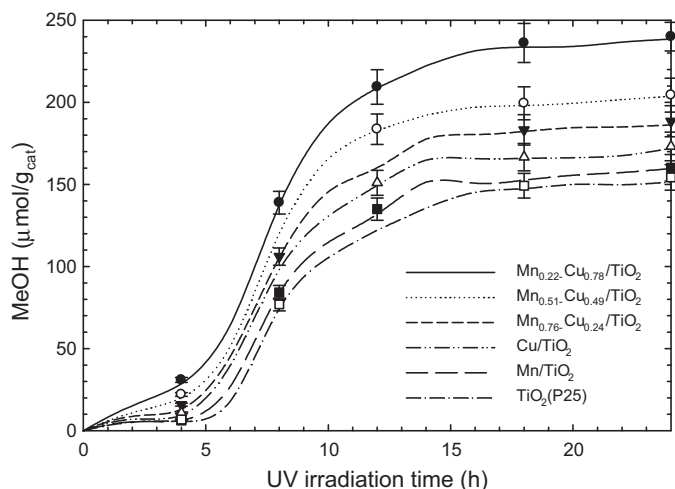


**Fig. 7.** Temporal evolution of methanol yield for different TiO<sub>2</sub> (P25), Mn/TiO<sub>2</sub>, Cu/TiO<sub>2</sub>, Mn<sub>0.22</sub>–Cu<sub>0.78</sub>/TiO<sub>2</sub>, Mn<sub>0.51</sub>–Cu<sub>0.49</sub>/TiO<sub>2</sub>, Mn<sub>0.76</sub>–Cu<sub>0.24</sub>/TiO<sub>2</sub> photocatalysts (0.5 g/L).

well-known to favor the arrangement of Fermi levels so the metal dopant acted as an electron trapper by avoiding the subsequent recombination of hole and electron. When coupled with manganese metal, this event is even promoted due to the rapid transport of high-energy electrons to the metal dopants thereby increasing the photocatalytic reduction of carbon dioxide to methanol.

In order to benchmark the photocatalytic conversion of CO<sub>2</sub>, the energy and quantum efficiencies were computed for the methanol production after 10 h of UV irradiation time. Bearing in mind that the energy efficiency is intimately connected with the conversion of electromagnetic energy into the chemical one, this is equivalent to the MeOH heat combustion. Table 3 shows the energy ( $\eta_{\text{energy}}$ ) and quantum ( $\eta_{\text{quantum}}$ ) efficiencies for TiO<sub>2</sub> (P25), Mn/TiO<sub>2</sub>, Cu/TiO<sub>2</sub>, Mn<sub>0.22</sub>–Cu<sub>0.78</sub>/TiO<sub>2</sub>, Mn<sub>0.51</sub>–Cu<sub>0.49</sub>/TiO<sub>2</sub>, Mn<sub>0.76</sub>–Cu<sub>0.24</sub>/TiO<sub>2</sub>, where one can identify the superior performance obtained with the Mn<sub>0.22</sub>–Cu<sub>0.78</sub>/TiO<sub>2</sub> specimen with 18.4 and 26.5%, respectively.

Fig. 8a and b shows the influence of copper loading on the conversion of carbon dioxide after 10 and 24 h irradiation time, while Fig. 9a and b depicts the effect of manganese loading at the same reaction times. As can be seen from Fig. 8a and b, the methanol production reached the maximum value of 190.1 μmol/g<sub>cat</sub> when the copper loading was 2.08% (w/w) and then decreased to 128.7 μmol/g<sub>cat</sub> for a copper loading of 4% (w/w) after 10 h UV irradiation time. Increasing further the reaction time up to 24 h, the photocatalytic yields in terms of methanol was 232.0 μmol/g<sub>cat</sub> for a copper loading of 2.1% (w/w) and reduced till 172.5 μmol/g<sub>cat</sub> for 4% (w/w). Additionally, Fig. 9a and b indicated that the maximum methanol yield was 188.9 μmol/g<sub>cat</sub> with a manganese loading 0.59% (w/w) and progressively decreased by adding more metal dopant exhibiting a MeOH production near 117.6 μmol/g<sub>cat</sub> for the highest manganese loading (4%, w/w) after 10 h UV irradiation time.

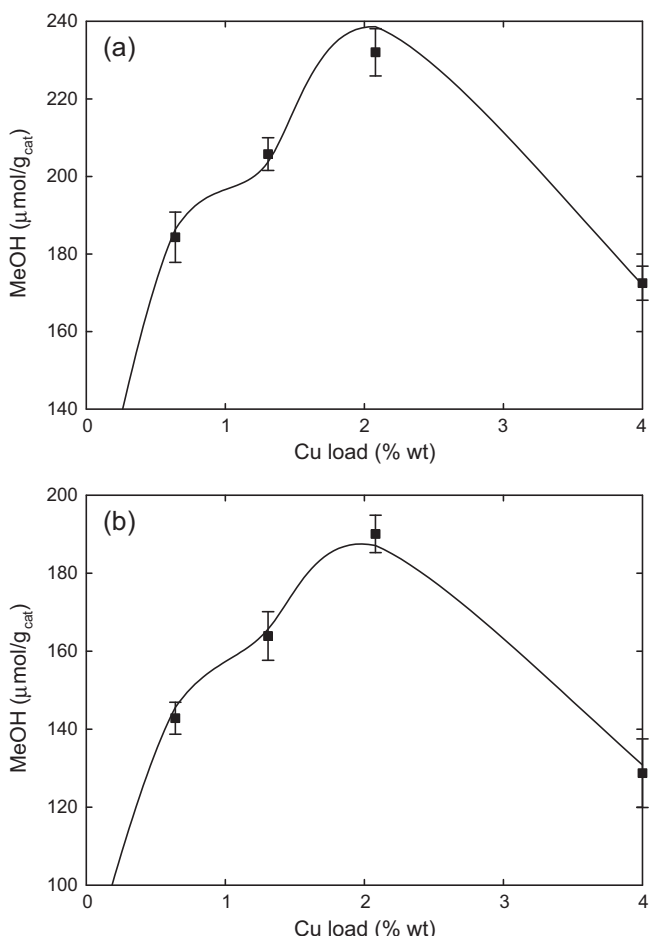


**Fig. 8.** Influence of copper loading on methanol yield after (a) 10 h and (b) 24 h UV irradiation time.

The final MeOH yields obtained after 24 h were 236.4 μmol/g<sub>cat</sub> for 0.59% (w/w) corresponding the maximum conversion, and gradually worsened to 155.5 μmol/g<sub>cat</sub> for a manganese loading of 4% (w/w).

The behavior depicted in both Figs. 8a and b and 9a and b underlined that excess copper and manganese loadings on the catalyst surface can mask the titania substrate thereby deteriorating the photocatalytic efficiency of titanium oxide. In a nutshell, an optimum molar ratio between manganese and copper metal dopants was found for the laboratory-made photocatalysts as evidenced by the experimental CO<sub>2</sub> conversions attained with the Mn<sub>0.22</sub>–Cu<sub>0.78</sub>/TiO<sub>2</sub> specimen. Similarly, the quantity of photocatalyst fed into the UV reactor was optimized accordingly as to prevent somewhat the concealment and suppression of UV radiation being dispersed within the UV photoreactor.

**Table 3**

MeOH yield after 10 and 24 h irradiation time, energy efficiency ( $\eta_{\text{energy}}$ ), and quantum efficiency ( $\eta_{\text{quantum}}$ ) for manganese- and copper-doped titania photocatalysts.

	MeOH   10 h (μmol/g <sub>cat</sub> )	MeOH   24 h (μmol/g <sub>cat</sub> )	$\eta_{\text{energy}}$	$\eta_{\text{quantum}}$
TiO <sub>2</sub> (P25)	105.3	151.6	0.96	5.29
Mn/TiO <sub>2</sub>	114.8	159.8	3.65	8.04
Cu/TiO <sub>2</sub>	130.8	172.0	6.43	19.01
Mn <sub>0.22</sub> –Cu <sub>0.78</sub> /TiO <sub>2</sub>	187.1	238.6	18.41	26.47
Mn <sub>0.51</sub> –Cu <sub>0.49</sub> /TiO <sub>2</sub>	165.7	203.8	12.08	23.65
Mn <sub>0.76</sub> –Cu <sub>0.24</sub> /TiO <sub>2</sub>	145.6	186.4	10.24	22.19

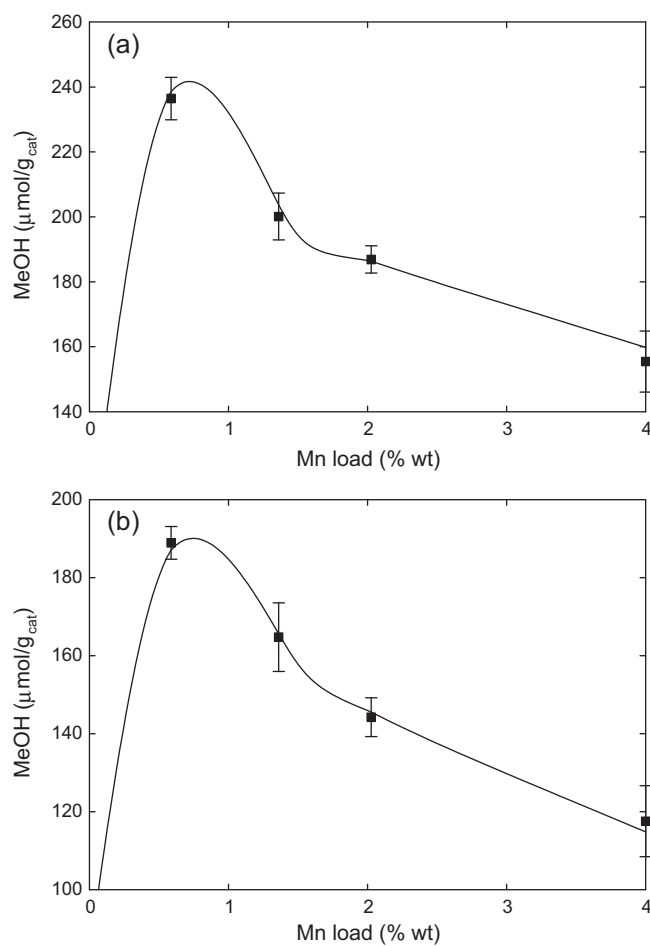


**Fig. 9.** Influence of manganese loading on methanol yield after (a) 10 h and (b) 24 h UV irradiation time.

#### 4. Conclusions

Manganese- and copper-doped titania laboratory-made catalysts synthetized by means of sol-gel process were comparatively evaluated with commercial TiO<sub>2</sub> (P25) for the photoreduction of carbon dioxide to methanol. XRD diffractograms has revealed nanocomposites owning the specific crystalline phases of TiO<sub>2</sub> (anatase/rutile), β-MnO<sub>2</sub> and Cu<sub>2</sub>O, which guaranteed the preservation of the initial titania structure. The morphological depiction from TEM patterns gave rise to the existence of Mn and Cu clusters deposited on the surface of titania substrate with typical grain sizes < 55 nm. This fact enabled superior efficiencies for the photocatalytic reduction of carbon dioxide as long as the particle size was in the range from 15 to 25 nm.

The higher bandgaps were obtained for the commercial catalyst, while the laboratory-made catalysts including Cu/TiO<sub>2</sub>, Mn<sub>0.22</sub>-Cu<sub>0.78</sub>/TiO<sub>2</sub>, Mn<sub>0.51</sub>-Cu<sub>0.49</sub>/TiO<sub>2</sub>, Mn<sub>0.76</sub>-Cu<sub>0.24</sub>/TiO<sub>2</sub> exhibited bandgaps lower than 3 eV. From the XPS spectra, the element

molar ratios of Mn- and Cu-doped photocatalysts have unveiled the same binding energies characteristic of pure Mn, Cu and Ti (2p<sub>3/2</sub>, 2p<sub>1/2</sub>), which allowed querying the structure and chemical composition of the nanocomposites. In addition, both metal dopants allow preserving the light absorption capacity of titanium oxide as evidenced from the DRS spectra for Mn- and Cu-doped titania specimens. Here, the coupling achieved between manganese and copper has been found to enhance the photocatalytic reduction of CO<sub>2</sub> to methanol due to the rapid transport of excited electrons to the metal dopants. Mn<sub>0.22</sub>-Cu<sub>0.78</sub>/TiO<sub>2</sub> exhibited the higher methanol yields as well as the higher quantum and energy efficiencies by highlighting the role exerted by the metal dopant acting as an electron trapper, thereby promoting the photocatalytic conversion of carbon dioxide.

#### Acknowledgment

The authors gratefully acknowledged the financial support of Fundação para a Ciência e Tecnologia, Portugal.

#### References

- [1] F. Barzaghi, F. Mani, M. Peruzzini, Energy & Environmental Science 2 (2009) 322–330.
- [2] B.P. Mandal, M. Kundu, S.S. Bandyopadhyay, Journal of Chemical and Engineering Data 50 (2005) 352–358.
- [3] J. Gabrielsen, M.L. Michelsen, E.H. Stenby, G.M. Kontogeorgis, Industrial & Engineering Chemistry Research 44 (2005) 3348–3354.
- [4] A.L. Chaffee, G.P. Knowles, Z. Liang, International Journal of Greenhouse Gas Control 1 (2007) 11–18.
- [5] R. Serna-Guerrero, E. Da'na, A. Sayari, Industrial & Engineering Chemistry Research 47 (2008) 9406–9412.
- [6] M.L. Druckenmiller, M.M. Maroto-Valer, Fuel Processing Technology 86 (2005) 1599–1614.
- [7] N. Liu, G.M. Bond, A. Abel, Fuel Processing Technology 86 (2005) 1615–1625.
- [8] A.D. Ebner, J.A. Ritter, Separation Science and Technology 44 (2009) 1273–1421.
- [9] V. Zelenák, M. Badanicová, D. Halamová, Chemical Engineering Journal 144 (2008) 336–342.
- [10] C. Song, Catalysis Today 115 (2006) 2–32.
- [11] I.H. Tseng, W.C. Chang, J.C.S. Wu, Applied Catalysis B: Environmental 37 (2002) 37–48.
- [12] K. Koci, V. Matejka, P. Kovar, Z. Lacny, L. Obalova, Catalysis Today 161 (2011) 105–109.
- [13] C.-C. Lo, C.-H. Hung, C.-S. Yuan, J.-F. Wu, Solar Energy Materials and Solar Cells 91 (2007) 1765–1774.
- [14] S.S. Tan, L. Zou, E. Hu, Catalysis Today 115 (2006) 269–273.
- [15] N. Sasirekha, S.J.S. Basha, K. Shanthi, Applied Catalysis B: Environmental 62 (2006) 169–180.
- [16] K. Teramura, H. Tsuneoka, T. Shishido, T. Tanaka, Chemical Physics Letters 467 (2008) 191–194.
- [17] K. Kočí, L. Obalová, L. Matějová, D. Plachá, Z. Lacný, J. Jirkovský, O. Šolcová, Applied Catalysis B: Environmental 89 (2009) 494–502.
- [18] Z. Zhao, J. Fan, S. Liu, Z. Wang, Chemical Engineering Journal 151 (2009) 134–140.
- [19] X.-H. Xia, Z.-J. Jia, Y. Yu, Y. Liang, Z. Wang, L.-L. Ma, Carbon 45 (2007) 717–721.
- [20] Y. Shioya, K. Ikeue, M. Ogawa, M. Anpo, Applied Catalysis A: General 254 (2003) 251–259.
- [21] H. Yamashita, Y. Fujii, Y. Ichihashi, S.G. Zhang, K. Ikeue, D.R. Park, K. Koyano, T. Tatsumi, M. Anpo, Catalysis Today 45 (1998) 221–227.
- [22] J.-S. Hwang, J.-S. Chang, S.-E. Park, K. Ikeue, M. Anpo, Studies in Surface Science and Catalysis 153 (2004) 299–302.
- [23] H. Yamashita, M. Okazaki, K. Ikeue, M. Anpo, Studies in Surface Science and Catalysis 153 (2004) 289–294.
- [24] K. Ikeue, S. Nozaki, M. Ogawa, M. Anpo, Catalysis Today 74 (2002) 241–248.
- [25] M. Matsuoka, M. Anpo, Journal of Photochemistry and Photobiology C: Photochemistry Reviews 3 (2003) 225–252.